

Macroscopic constitutive law for Mastic Asphalt Mixtures from multiscale modeling

Richard Valenta^b, Michal Šejnoha^{a,b,*}, Jan Zeman^a

^a*Department of Mechanics, Faculty of Civil Engineering, Czech Technical University in Prague, Thákurova 7, 166 29 Prague 6, Czech Republic*

^b*Centre for Integrated Design of Advances Structures, Thákurova 7, 166 29 Prague 6, Czech Republic*

Abstract

A well established framework of an uncoupled hierarchical modeling approach is adopted here for the prediction of macroscopic material parameters of the Generalized Leonov (GL) constitutive model intended for the analysis of flexible pavements at both moderate and elevated temperature regimes. To that end, a recently introduced concept of a statistically equivalent periodic unit cell (SEPUC) is addressed to reflect a real microstructure of Mastic Asphalt mixtures (MAM). While mastic properties are derived from an extensive experimental program, the macroscopic properties of MAM are fitted to virtual numerical experiments performed on the basis of first order homogenization scheme. To enhance feasibility of the solution of the underlying nonlinear problem a two-step homogenization procedure is proposed. Here, the effective material properties are first found for a mortar phase, a composite consisting of a mastic matrix and a fraction of small aggregates. These properties are then introduced in place of the matrix in actual unit cells to give estimates of the model parameters on macroscale. Comparison with the Mori-Tanaka predictions is also provided suggesting limitations of classical micromechanical models.

Key words: Mastic Asphalt mixture, multiscale analysis, binary image, periodic unit cell, homogenization, Generalized Leonov model

* Corresponding author. Tel.: +420-2-2435-4494; fax +420-2-2431-0775
Email addresses: richard.valenta@centrum.cz (Richard Valenta),
 sejnom@fsv.cvut.cz (Michal Šejnoha), zemanj@cml.fsv.cvut.cz (Jan Zeman).

1 Introduction

As seen in Fig. 1(a), asphalt mixtures represent in general a highly heterogeneous material with complex microstructure consisting at minimum of mastic binder, aggregates and voids. When limiting our attention to Mastic Asphalt mixtures, used typically in traffic arteries of substantial importance, the fraction of voids becomes negligible. A binary image of such a two-phase material system plotted in Fig. 1(b) is then readily available. The literature offers several distinct routes taking advantage of such a representation.

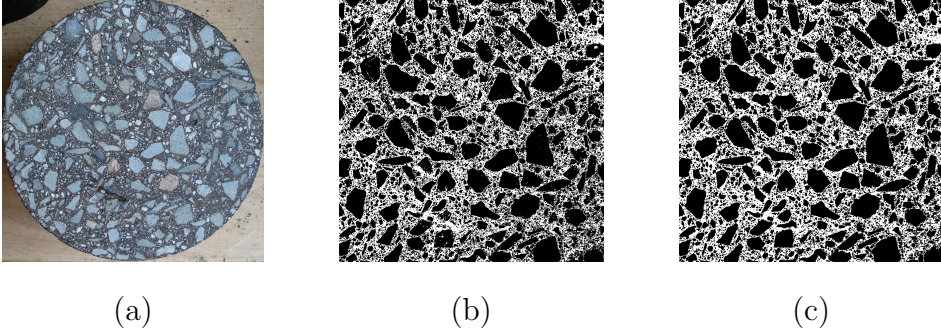


Fig. 1. (a) A real microstructure of an asphalt mixture, (b) Original binary image, (c) Improved binary image

Phenomenological constitutive models enhanced by introducing a microstructure linked aggregate distribution tensor [1,2] were proposed, following the footsteps of isotropic viscoelastic or viscoplastic models developed since the early 1990s [3,4,5,6,7, to cite a few], to account for an intrinsic aggregate structure anisotropy. Recently, detailed micromechanical models developed on the basis of image processing of either two-dimensional digital photography or three-dimensional X-ray computed tomography have been favored for the performance assessment of asphalt concrete composites. Typically, a sufficiently large sample of microstructure of a two-phase composite system, transformed into a binary image, was adopted to serve as a representative volume element (RVE). Either direct application of these models [8,9,10] or application of simplified artificial microstructures of the same type [11] was examined to provide estimates of the macroscopic response. While capturing both the local and overall behavior sufficiently accurately, most of these models suffer from computational inefficiency. Exploitation of the true potential of classical averaging micromechanical schemes combined with “bottom-up” hierarchical homogenization technique thus appears rather natural. As an example we recall a successful application of the Mori-Tanaka method in upscaling viscoelastic properties of asphalt mixtures at low temperatures [12,13,14,15].

Growing from the roots planted by the authors in the early 2000s [16,17,18] the present contribution combines these various aspects of micromechanical modeling into a relatively simple, yet reliable and efficient computational scheme.

While still incorporating the prominent “bottom-up” uncoupled multiscale homogenization scheme, the effective properties on individual scales are found as volume averages of local stress and strain fields developed inside the so-called Statistically Equivalent Periodic Unit Cell [19].

Rendering the desired macroscopic constitutive model that describes the homogenized response of MAm to general loading actions thus endeavors to the formulation of a suitable micromechanical model on individual scales and to associated experimental work being jointly the building blocks of the upscaling procedure. Three particular scales shown in Fig. 2 are considered in the present study:

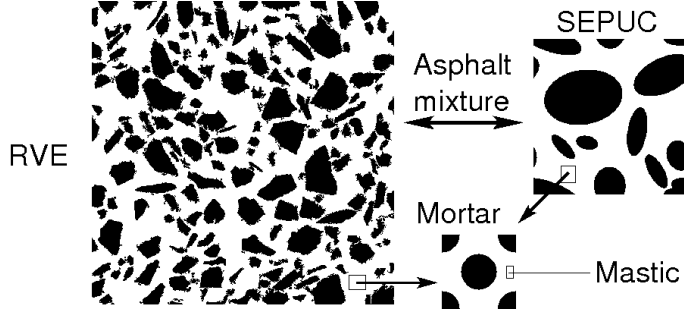


Fig. 2. Three distinct scales of Mastic Asphalt mixture

- Although the mastic-phase itself is a composite consisting of a filler and a bituminous binder, it is assumed in the present study to be well represented by a temperature and rate dependent homogeneous isotropic material. Since limiting our attention to elevated temperatures exceeding 30°C , the GL model discussed in Section 3.1 is exploited to provide for experimentally observed nonlinear viscoelastic behavior of bituminous matrices. The required experimental program to calibrate the model parameters is outlined in Section 3.2.
- As presented in Section 2.1, the mortar-phase naturally arises through the process of removing aggregates from original microstructure, Fig. 1(b), passing 2.26 mm sieve. Introducing the principal assumption of the adopted upscaling procedure - the GL model is suitable for governing the homogenized response on every scale - allows us to derive the model parameters on the mortar-scale by running a set of virtual numerical experiments on the simplified periodic hexagonal array model plotted in Fig. 2. The selection of this geometrical representation of the mortar composite is purely an assumption building upon the conclusion that at least for the mastic-phase and low-temperature creep the response is independent of the filler shape and mineralogy [13]. Various computational strategies delivering the searched macroscopic response are presented in Sections 2.2.1 - 2.2.3.
- The SEPUC, also seen in Fig. 2, is selected to predict the macroscopic response of MAm, where large aggregates are bonded to a mortar-phase being homogeneous and isotropic. The elliptical shape of aggregates has already

been successfully used in detailed micromechanical simulations presented in [11]. The issue of constructing SEPUC for the class of Mastic Asphalt mixtures is briefly addressed in Section 2.3.

- The proposed upscaling procedure consistent with Fig. 2 is then applied in Sections 3.3 and 3.4 to deliver the necessary parameters of the homogenized GL model.

In the following text, \mathbf{a} , \mathbf{a} and \mathbf{A} denote a vector, a symmetric second-order and a fourth-order tensor, respectively. The standard summation notation is adopted, i.e., $\mathbf{A} : \mathbf{B}$ and $\mathbf{A} : \mathbf{b}$ denote the sums $A_{ijkl}B_{klrs}$ and $A_{ijkl}b_{kl}$, $\mathbf{a} : \mathbf{b}$ being $a_{ij}b_{ij}$ represents a scalar quantity and $\mathbf{a} \cdot \mathbf{b}$ stands for $a_{ij}b_j$, where the summation with respect to repeated indices is used. The symbol $\{\mathbf{a}\}$ is reserved for a column matrix or a vectorial representation of symmetric second-order tensor while the notation $[\mathbf{L}]$ is employed for a matrix representation of a fourth-order tensor [20].

2 Concept of statistically equivalent periodic unit cell

It has been demonstrated in our previous work, see e.g. [17,21,22] that image analysis of real, rather than artificial, material systems plays an essential role in the derivation of a reliable and accurate computational model. This issue is revisited here to get, although considerably simplified, a reasonably accurate computational model (RVE→SEPUC) representing the real microstructure of Mastic Asphalt mixtures.

2.1 From real microstructure to computationally feasible RVE

Notice a $1,600 \times 1,600$ pixel resolution binary image in Fig. 1(b) created through the process of color segmentation of the original image in Fig. 1(a) using the freeware graphical software GIMP. Visible flaws, e.g. defects inside large aggregates, required, however, further modification. To that end, an automated numerical tool was developed to determine a boundary of each aggregate, fill defects inside large aggregates and separate all aggregates as much as possible. The resulting improved image seen in Fig. 1(c) then allows for microstructure quantification in terms of various statistical descriptors.

To open this subject, we consider first cumulative distribution functions of aggregates plotted in Fig. 3. The two graphs suggest a relatively large amount of small stones (cumulative distribution function of number of aggregates) which might seem, at least from their volume fraction point of view (cumulative distribution function of volume fraction of aggregates), almost negligible.

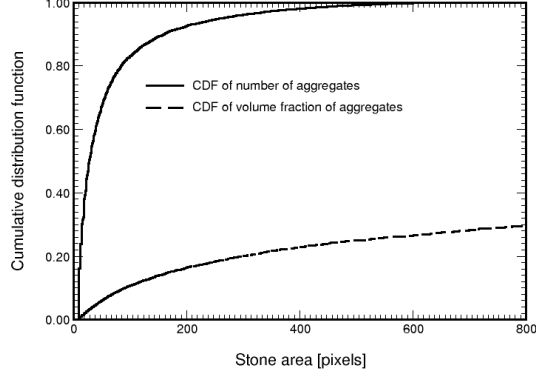


Fig. 3. Cumulative distribution function

Eliminating the small aggregates to simplify the original microstructure is naturally promoted. Several examples of such microstructures appear in Fig. 4. If admitting removal of all fragments smaller than 1,200 pixels in area (aggregates passing 2.36mm sieve) we reduce the total number of stones by 97% while the original volume fraction of aggregates dropped down only by 21%. However, neglecting the small aggregates completely would severely underestimate the final macroscopic predictions. A two-scale homogenization approach is therefore inevitable.

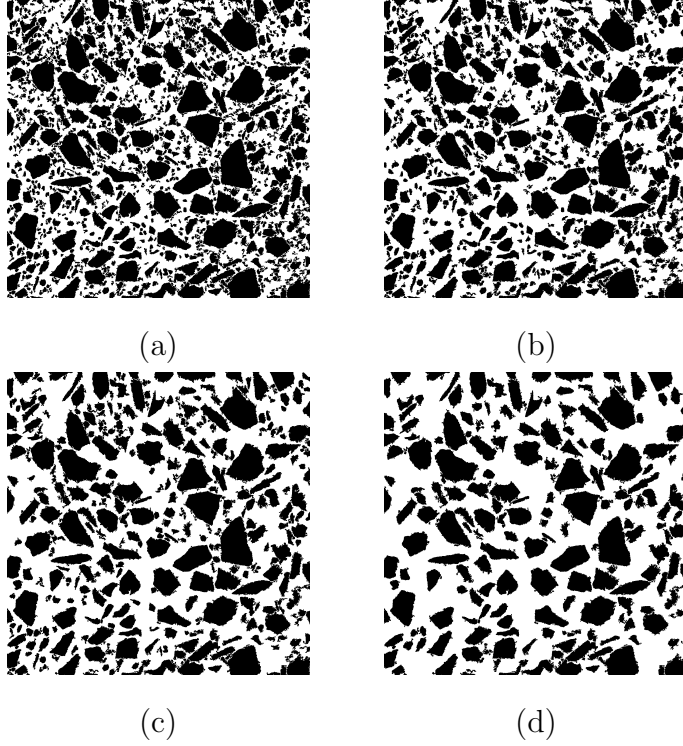


Fig. 4. Examples of binary images of original microstructure after eliminating stone fragments smaller than (in area): (a) 150px, (b) 300px, (c) 600px, (d) 1200px

2.2 Upscaling material properties towards Mastic Asphalt Mixes

Suppose that the microstructure in Fig. 4(d) is sufficient to provide reasonably accurate predictions of macroscopic response of MAm. With reference to Fig. 2 and to findings presented in [13] we further assume the mortar phase to be well represented by a periodic hexagonal arrangement of aggregates of a circular cross-section. The resulting Mastic Asphalt mixture then consists of 41% volume of large aggregates and 59% volume of mortar phase, whereas the mortar-mastic composite was calculated to have 34% volume of small stones and 64% volume of mastic phase. The latter composite is shown in Fig. 5(d). For further reference the subscript s will be reserved for aggregates (stones) whereas the subscript m will be used to denote the binder (either mortar or mastic matrix).

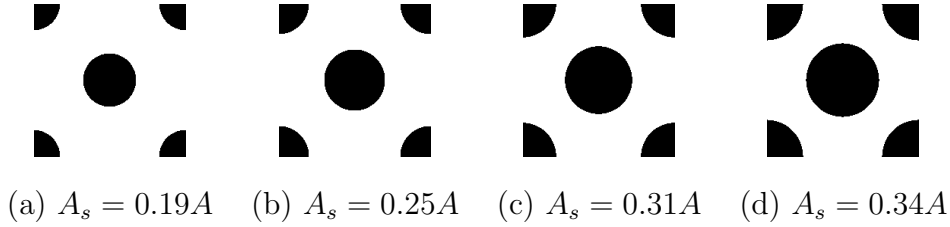


Fig. 5. PUC of mortar phase containing stone fragments smaller than (in area): (a) 150px, (b) 300px, (c) 600px, (d) 1200px

Given the geometrical models for individual scales now opens the way to the derivation of the effective elastic properties of MAm employing the uncoupled “bottom-up” upscaling scheme. While confirming applicability of this approach, these results will further serve as a point of departure for generating the statistically equivalent periodic unit cells and at the same time will provide a source of data to check the quality of the results obtained for these artificial microstructures, see Section 2.3.

A number of homogenization techniques is available in the literature. Three particular representatives will be now briefly reviewed. Owing to the solution of the underlying nonlinear viscoelastic problem, the formulation will be presented in an incremental format.

2.2.1 The Mori-Tanaka method

Consider a two-phase composite medium Ω loaded on its outer boundary S by an affine displacement field $\Delta \mathbf{u}_0 = \Delta \mathbf{E} \cdot \mathbf{x}$ consistent with the macroscopic uniform strain increment $\Delta \mathbf{E}$. The local constitutive equation can be written as

$$\Delta \boldsymbol{\sigma}(\mathbf{x}) = \mathbf{L}(\mathbf{x}) : \Delta \boldsymbol{\varepsilon}(\mathbf{x}) + \Delta \boldsymbol{\lambda}(\mathbf{x}) \quad \text{or} \quad \Delta \boldsymbol{\sigma}_r = \mathbf{L}_r : \Delta \boldsymbol{\varepsilon}_r + \Delta \boldsymbol{\lambda}_r, \quad (1)$$

when limiting our attention to a piecewise uniform variation of the stress and strain fields within individual phases; \mathbf{L}_r is then the stiffness tensor of the phase $r = s, m$ and the increment of eigenstress $\Delta\boldsymbol{\lambda}_r$ represents contributions caused by various non-mechanical physical sources. In the present study we admit only the creep strains developed in the binder phase thus leaving the aggregates to remain linearly elastic. In the framework of Dvorak's Transformation Field Analysis [23,24] the local strain increments then read

$$\Delta\boldsymbol{\varepsilon}_s = \mathbf{A}_s : \Delta\mathbf{E} + \mathbf{D}_{sm} : \Delta\boldsymbol{\mu}_m, \quad (2)$$

$$\Delta\boldsymbol{\varepsilon}_m = \mathbf{A}_m : \Delta\mathbf{E} + \mathbf{D}_{mm} : \Delta\boldsymbol{\mu}_m, \quad (3)$$

where $\mathbf{A}_r, \mathbf{D}_{rm}, r = s, m$, are the mechanical strain localization tensors and transformation influence functions, respectively. The phase eigenstrain $\boldsymbol{\mu}_m$ is introduced to account for a nonlinear viscoelastic behavior of the binder. Note that for a two-phase medium, the transformation influence functions are directly available in terms of the strain localization tensors [23].

Next, writing the macroscopic constitutive law as

$$\Delta\boldsymbol{\Sigma} = \mathbf{L}^{\text{hom}} : \Delta\mathbf{E} + \Delta\boldsymbol{\Lambda}, \quad (4)$$

and realizing that

$$\Delta\boldsymbol{\Sigma} = c_s \Delta\boldsymbol{\sigma}_s + c_m \Delta\boldsymbol{\sigma}_m, \quad (5)$$

yields the macroscopic stiffness matrix and the macroscopic eigenstress [23] as

$$\mathbf{L}^{\text{hom}} = c_s \mathbf{L}_s : \mathbf{A}_s + c_m \mathbf{L}_m : \mathbf{A}_m, \quad (6)$$

$$\begin{aligned} \Delta\boldsymbol{\Lambda} &= - \underbrace{[c_s (\mathbf{L}_s : \mathbf{D}_{sm} : \mathbf{M}_m) + c_m (\mathbf{L}_m : \mathbf{D}_{mm} : \mathbf{M}_m)]}_{=0} : \Delta\boldsymbol{\lambda}_m + c_m \Delta\boldsymbol{\lambda}_m, \\ &= c_m \boldsymbol{\lambda}_m = -c_m \mathbf{L}_m \boldsymbol{\mu}_m. \end{aligned} \quad (7)$$

Herein, the strain localization tensors \mathbf{A}_r are found from the Mori-Tanaka (MT) method [25]. In Benveniste's reformulation [26], the method approximates the particle interactions by loading an isolated heterogeneity bonded to an unbounded matrix by a uniform stress or strain found in the matrix. Introducing the partial strain concentration (localization) tensor \mathbf{T}_s for the phase s (note that $\mathbf{T}_m = \mathbf{I}$, the identity tensor), the local strain increment in aggregates is, in the absence of inelastic effects, provided by

$$\Delta\boldsymbol{\varepsilon}_s = \mathbf{T}_s : \Delta\boldsymbol{\varepsilon}_m. \quad (8)$$

Next, writing $\Delta\mathbf{E} = c_s \Delta\boldsymbol{\varepsilon}_s + c_m \Delta\boldsymbol{\varepsilon}_m$ readily provides

$$\Delta\boldsymbol{\varepsilon}_m = [c_m \mathbf{I} + c_s \mathbf{T}_s]^{-1} : \Delta\mathbf{E}, \quad (9)$$

$$\Delta\boldsymbol{\varepsilon}_s = (\mathbf{T}_s : \mathbf{A}_m) : \Delta\mathbf{E}, \quad (10)$$

which gives the strain localization tensors in the form

$$\mathbf{A}_m = [c_m \mathbf{I} + c_s \mathbf{T}_s]^{-1} \quad \mathbf{A}_s = \mathbf{T}_s : \mathbf{A}_m. \quad (11)$$

Closed form solutions for the localization tensor \mathbf{T}_s are provided in the literature for certain types of heterogeneities, see e.g. [27]. Here, the model of aligned infinite cylinders of circular cross-sections, consistent with the assumed plane strain conditions, is adopted. Since used later in the Appendix, we present here the homogenized in-plane shear modulus m in the form

$$m_{\text{MT}} = \frac{m_s m_m (k_m + 2m_m) + k_m m_m (c_s m_s + c_m m_m)}{k_m m_m + (k_m + 2m_m)(c_s m_m + c_m m_s)}, \quad (12)$$

where $m_r, r = s, m$ are corresponding shear moduli of individual phases. If both phases are also isotropic we get $k_r = m_r / (1 - 2\nu_r)$, where ν_r is the Poisson ratio. Finally note that all localization and transformation tensors mentioned in this section are functions of the instantaneous material properties of the binder phase, the current value of the viscoelastic shear modulus in particular.

2.2.2 The Fast Fourier Transform method

The Fast Fourier Transform (FFT) method proposed in [28] can be imagined as a passage between classical micromechanics models and the concept of periodic homogenization. To introduce this approach consider again a two-phase composite medium subjected to the same boundary conditions as in the previous section.

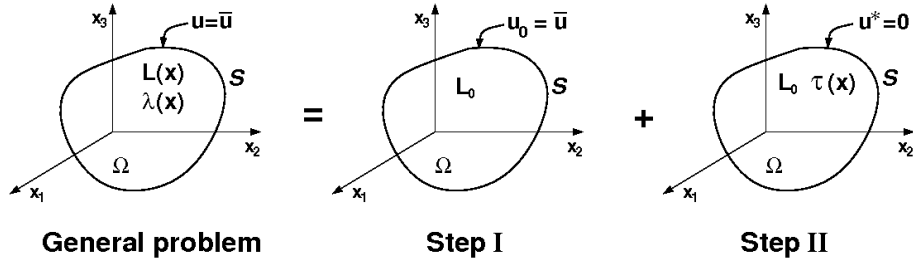


Fig. 6. Body with prescribed surface displacements including eigenstresses

As suggested by Hashin and Shtrikman [29] the local stress and strain fields in Eq. (1)₁ can be found from two auxiliary boundary value problems, Fig. 6. The procedure starts by assuming a geometrically identical body with a certain reference homogeneous, but generally anisotropic, medium \mathbf{L}_0 and the same prescribed displacements. The corresponding uniform strain \mathbf{E} and stress $\mathbf{\Sigma}$ fields are related through constitutive law as

$$\Delta \mathbf{\Sigma} = \mathbf{L}_0 : \Delta \mathbf{E} \text{ in } \Omega, \quad \Delta \mathbf{u}_0 = \Delta \bar{\mathbf{u}} \text{ on } S. \quad (13)$$

Following the Hashin-Shtrikman idea, we introduce the symmetric stress polarization tensor $\boldsymbol{\tau}$ such that

$$\Delta\boldsymbol{\sigma}(\mathbf{x}) = \mathbf{L}_0 : \Delta\boldsymbol{\varepsilon}(\mathbf{x}) + \Delta\boldsymbol{\tau}(\mathbf{x}). \quad (14)$$

In addition, denote

$$\mathbf{u}^* = \mathbf{u} - \mathbf{u}_0 \text{ in } \Omega, \mathbf{u}^* = \mathbf{0} \text{ on } S, \boldsymbol{\varepsilon}^* = \boldsymbol{\varepsilon} - \mathbf{E}, \text{ in } \Omega. \quad (15)$$

The increment of stress polarization tensor $\boldsymbol{\tau}$ then becomes

$$\Delta\boldsymbol{\tau}(\mathbf{x}) = (\mathbf{L}(\mathbf{x}) - \mathbf{L}_0) : \Delta\boldsymbol{\varepsilon}(\mathbf{x}) - \Delta\boldsymbol{\lambda}(\mathbf{x}). \quad (16)$$

If the polarization stress is known, the fluctuation part of the strain field $\boldsymbol{\varepsilon}^*$ can be obtained via Green's function $\boldsymbol{\Gamma}^0$ for a given reference medium in the form, see e.g. [30,28],

$$\Delta\boldsymbol{\varepsilon}^*(\mathbf{x}) = - \int_{\Omega} \boldsymbol{\Gamma}^0(\mathbf{x} - \mathbf{x}') : \Delta\boldsymbol{\tau}(\mathbf{x}') d\mathbf{x}'. \quad (17)$$

Combining Eqs. (15)₃, (16) and (17) we obtain the so called *periodic Lippmann Schwinger* integral equation for a given reference medium as

$$\Delta\boldsymbol{\varepsilon}(\mathbf{x}) + \int_{\Omega} \boldsymbol{\Gamma}^0(\mathbf{x} - \mathbf{x}') : [(\mathbf{L}(\mathbf{x}') - \mathbf{L}_0) : \Delta\boldsymbol{\varepsilon}(\mathbf{x}') - \Delta\boldsymbol{\lambda}(\mathbf{x}')] d\mathbf{x}' = \Delta\mathbf{E}. \quad (18)$$

This equation can be solved by the following iterative procedure

$$\Delta\boldsymbol{\varepsilon}^{k+1}(\mathbf{x}) = \Delta\mathbf{E} - \int_{\Omega} \boldsymbol{\Gamma}^0(\mathbf{x} - \mathbf{x}') : [(\mathbf{L}(\mathbf{x}') - \mathbf{L}^0) : \Delta\boldsymbol{\varepsilon}^k(\mathbf{x}') - \Delta\boldsymbol{\lambda}^k(\mathbf{x}')] d\mathbf{x}'. \quad (19)$$

Typically, the Fast Fourier Transform (or rather its discrete version when dealing directly with binary images) is employed to solve the above equation. Details on actual numerical implementation can be found in [28]. In the absence of inelastic effects the above equation simplifies as

$$\boldsymbol{\varepsilon}^{k+1}(\mathbf{x}) = \mathbf{E} - \int_{\Omega} \boldsymbol{\Gamma}^0(\mathbf{x} - \mathbf{x}') : [(\mathbf{L}(\mathbf{x}') - \mathbf{L}^0) : \boldsymbol{\varepsilon}^k(\mathbf{x}')] d\mathbf{x}'. \quad (20)$$

For plane-strain problem the homogenized elastic stiffness matrix \mathbf{L}^{hom} can be found from the solution of four successive elasticity problems. To that end, the RVE is loaded, in turn, by each of the four components of \mathbf{E} , while the other three components vanish. The volume stress averages normalized with respect to \mathbf{E} then furnish individual columns of \mathbf{L}^{hom} .

2.2.3 First order homogenization of periodic fields

Consider a material representative volume element now defined in terms of a periodic unit cell (PUC). Similar to the previous sections, suppose that the

PUC is subjected to boundary displacements $\Delta \mathbf{u}_0$ resulting in a uniform strain $\Delta \mathbf{E}$ throughout the body. The strain and displacement fields in the PUC then admit the following decomposition, recall also Eq. (15)₃,

$$\Delta \mathbf{u}(\mathbf{x}) = \Delta \mathbf{E} \cdot \mathbf{x} + \Delta \mathbf{u}^*(\mathbf{x}), \quad \forall \mathbf{x} \in \Omega, \quad \mathbf{u} = \mathbf{u}_0 \quad \forall \mathbf{x} \in S, \quad (21)$$

$$\Delta \boldsymbol{\varepsilon}(\mathbf{x}) = \Delta \mathbf{E} + \Delta \boldsymbol{\varepsilon}^*(\mathbf{x}), \quad \forall \mathbf{x} \in \Omega. \quad (22)$$

The first term in Eq. (21) corresponds to a displacement field in an effective homogeneous medium with the same overall properties as the composite. The fluctuation part \mathbf{u}^* enters Eq. (21) as a consequence of the presence of heterogeneities and has to disappear upon volume averaging, see [31] for further discussion. This condition is met for any periodic displacement field with the period equal to the size of the unit cell under consideration, [32, and references therein]. The periodicity of \mathbf{u}^* further implies that the average of $\boldsymbol{\varepsilon}^*$ in the unit cell vanishes as well. Hence

$$\langle \boldsymbol{\varepsilon}(\mathbf{x}) \rangle = \mathbf{E} + \langle \boldsymbol{\varepsilon}^*(\mathbf{x}) \rangle, \quad \langle \boldsymbol{\varepsilon}^*(\mathbf{x}) \rangle = \frac{1}{\Omega} \int_{\Omega} \boldsymbol{\varepsilon}^*(\mathbf{x}) \, d\mathbf{x} = \mathbf{0}. \quad (23)$$

Derivation of the macroscopic response then relies on the application of Hill's lemma [33]. We now introduce a slight inconsistency in the present formulation and assume that uniform tractions $\Delta \mathbf{p}_0$ (consistent with the macroscopic stresses $\Delta \boldsymbol{\Sigma}$, $\Delta \mathbf{p}_0 = \Delta \boldsymbol{\Sigma} \cdot \mathbf{n}$, \mathbf{n} being the unit outward normal to the boundary of the PUC) rather than displacements are prescribed to get

$$\langle \delta \boldsymbol{\varepsilon} : \Delta \boldsymbol{\sigma}(\mathbf{x}) \rangle = \delta \mathbf{E} : \Delta \boldsymbol{\Sigma}. \quad (24)$$

Substituting the discretized form of the local strain increment $\{\Delta \boldsymbol{\varepsilon}(\mathbf{x})\} = \{\Delta \mathbf{E}\} + [\mathbf{B}] \{\Delta \mathbf{r}^*\}$ together with local constitutive equation (1)₁ into Eq. (24) gives

$$\begin{bmatrix} \frac{1}{\Omega} \int_{\Omega} [\mathbf{L}(\mathbf{x})] \, d\Omega & \frac{1}{\Omega} \int_{\Omega} [\mathbf{L}(\mathbf{x})] [\mathbf{B}] \, d\Omega \\ \frac{1}{\Omega} \int_{\Omega} [\mathbf{B}]^T [\mathbf{L}(\mathbf{x})] \, d\Omega & \frac{1}{\Omega} \int_{\Omega} [\mathbf{B}]^T [\mathbf{L}(\mathbf{x})] [\mathbf{B}] \, d\Omega \end{bmatrix} \begin{Bmatrix} \{\Delta \mathbf{E}\} \\ \{\Delta \mathbf{r}^*\} \end{Bmatrix} = \begin{Bmatrix} \{\Delta \boldsymbol{\Sigma}\} - \frac{1}{\Omega} \int_{\Omega} \{\Delta \boldsymbol{\lambda}\} \, d\Omega \\ -\frac{1}{\Omega} \int_{\Omega} [\mathbf{B}]^T \{\Delta \boldsymbol{\lambda}\} \, d\Omega \end{Bmatrix}. \quad (25)$$

Recall that in the framework of finite element method the matrix $[\mathbf{B}]$ is often termed the geometrical matrix and the vector $\{\Delta \mathbf{r}^*\}$ stores the increments of the fluctuation nodal displacements. Finally, after rewriting the above equation as

$$\begin{bmatrix} [\mathbf{K}]_{11} & [\mathbf{K}]_{12} \\ [\mathbf{K}]_{21} & [\mathbf{K}]_{22} \end{bmatrix} \begin{Bmatrix} \{\Delta \mathbf{E}\} \\ \{\Delta \mathbf{r}^*\} \end{Bmatrix} = \begin{Bmatrix} \{\Delta \boldsymbol{\Sigma}\} + \{\Delta \mathbf{F}^0\} \\ \{\Delta \mathbf{f}^0\} \end{Bmatrix}, \quad (26)$$

and eliminating the fluctuating displacements vector $\{\Delta \mathbf{r}^*\}$ we arrive at the incremental form of the macroscopic constitutive law

$$\{\Delta \boldsymbol{\Sigma}\} = [\mathbf{L}^{\text{hom}}] \{\Delta \mathbf{E}\} + \{\Delta \boldsymbol{\Lambda}\}, \quad (27)$$

where

$$[\mathbf{L}^{\text{hom}}] = ([\mathbf{K}]_{11} - [\mathbf{K}]_{12} [\mathbf{K}]_{22}^{-1} [\mathbf{K}]_{12}^T), \quad \{\Delta \Lambda\} = -\{\Delta F^0\} + ([\mathbf{K}]_{12} [\mathbf{K}]_{22}^{-1} \{\Delta f^0\}).$$

Also note that, when returning back to our original formulation with the prescribed overall strain only, the system of equations (26) reduces to

$$[\mathbf{K}]_{22} \{\Delta \mathbf{r}^*\} = -[\mathbf{K}]_{21} \{\Delta \mathbf{E}\} + \{\Delta \mathbf{f}^0\}. \quad (28)$$

2.2.4 Effective properties from binary images

A simple example of a two-scale elastic homogenization, recall Fig. 2, is presented here for the binary images plotted in Figs. 4 and 5. Both the aggregates and mastic are assumed to be isotropic. The elastic modulus of the mastic phase being equal to 1,600 MPa ($\nu_m = 0.4$) is associated with the value of the storage modulus at zero value of the loss modulus based on the Cole Cole graph in Fig. 10(d). The elastic material properties of aggregates are considered to be those of a spilite rock with the elastic modulus equal to 60,000 MPa ($\nu_s = 0.2$).

Table 1

Effective properties of mortar matrix

PUC (Fig. 5)	(a)	(b)	(c)	(d)	FEM (d)	MT (d)
E^{hom} [MPa]	2443	2670	2897	3150	3145	3462
ν^{hom} [-]	0.38	0.38	0.38	0.38	0.38	38

Since dealing directly with the binary representation of real microstructures the FFT method was adopted in this study. The homogenized material properties on the mortar scale are listed in Table 1. Note that due to an hexagonal arrangement of stones within the PUC the transverse material isotropy was generated. In the second homogenization the effective properties of the mortar are then used in place of the original mastic matrix when treating individual RVEs in Fig. 4. The final results, promoting the proposed two-step upscaling homogenization scheme, appear as dash-pattern columns in Fig. 7. Also notice the checkerboard columns, derived for the same microstructures but using mastic material properties for the binder, clearly indicating a considerable impact of eliminated stones on the predicted effective properties.

2.3 Statistically equivalent periodic unit cell

Although considerable savings in computational time can be achieved with coarse RVEs, the analysis employing original microstructures still presents a significant challenge particularly in view of a large scale nonlinear analysis of

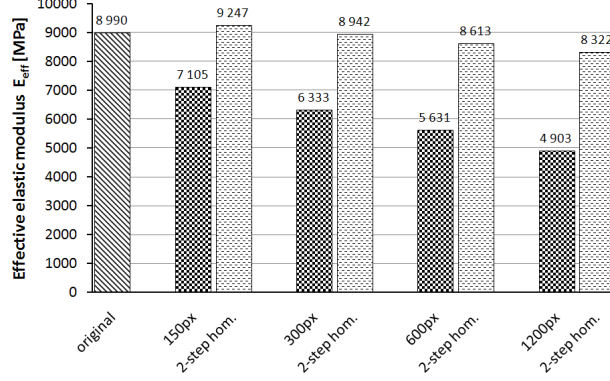


Fig. 7. Effective elastic modulus derived from images in Fig. 4

multi-layered rodes carried out, possibly, in the framework of multiscale FE^2 analysis [34,35]. Even at moderate temperatures the stiffness of the binder might reduce by several orders of magnitude resulting in a drastic mismatch between the elastic moduli of binder and aggregates and consequently in a poor convergence performance of the FFT method. Although some improvements to the original formulation exist, they will not be considered in the present study. Instead a rather different route is built taking account of the so called statistically equivalent periodic unit cell [17].

In particular, suppose that the original microstructure can be replaced by a certain artificial periodic unit cell that, from the microstructure point of view, statistically resembles the real material system in terms of, e.g. the two-point probability function, see e.g. [36] for in depth discussion on various statistical descriptors. Such a unit cell can be defined by the following parameters: number of aggregates having elliptical shape, size, position, orientation and aspect ratio of the axes of individual ellipses. The size of stones is derived based on the cumulative distribution function in Fig. 3. For example, if 10 stones are selected for a PUC then the smallest stone corresponds to an average size of 10% of the smallest stones determined from the cumulative distribution function. The next stone then reflects the size of the subsequent 10% stones, etc. Examples of such unit cells are depicted in Fig. 8.

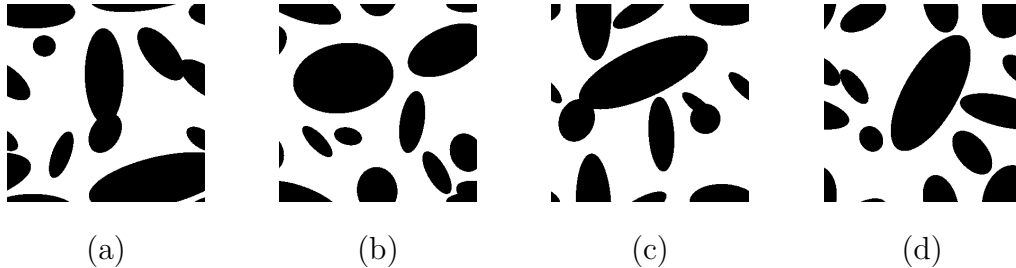


Fig. 8. Examples of SEPUCs corresponding to a binary image in Fig. 4(d): (a) SEPUC 6, (b) SEPUC 37, (c) SEPUC 43, (d) SEPUC 48

These unit cells were derived by matching the two-point probability function of the original microstructure, Fig. 3(d), and the SEPUC. The underlying op-

timization problem was solved with the help of the evolutionary algorithm GRADE [37,38]. See also [17,16] for other applications of genetic algorithm based solution strategies. It is worth mentioning that no interpenetration constrain was introduced as it was naturally enforced through the consistency of volume fractions of aggregates in the SEPUC and targeted microstructure in Fig. 3(d).

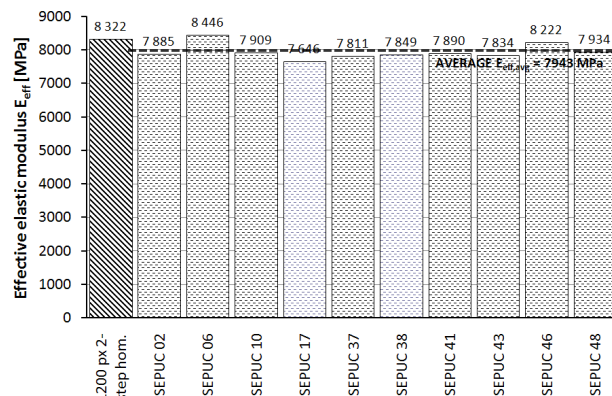


Fig. 9. Effective elastic modulus derived from SEPUCs in Fig. 7

As typical of genetic algorithms based optimization procedures, each run results in a unique SEPUC with a slightly different arrangement of stones, see Fig. 8. It therefore remains to confirm that all cells provide the “same” macroscopic response. Note that for the sake of efficiency the target microstructure in Fig. 3(d) with mastic binder being replaced by mortar phase (the fourth column in Table 1) was used when generating artificial periodic microstructures. The corresponding effective properties are represented by the first column in Fig. 9. The remaining columns refer to the effective elastic modulus for the selected SEPUCs (100 such cells were generated). Although slightly different in their geometrical details they all provide nearly the same macroscopic response almost identical to the original microstructure.

Table 2

Effective properties of asphalt

SEPUC (Fig. 8)	(a)	(b)	(c)	(d)	MT (d)	Fig. 3(d)	Fig. 1(c)
E^{hom} [MPa]	8446	7811	7934	7834	7426	8322	8998
ν^{hom} [-]	0.33	0.35	0.33	0.33	0.33	0.32	0.31

The Mori-Tanaka prediction found from the same upscaling procedure assuming aggregates to be represented by statistically uniform distribution of circular cylinders is also presented and compared in Table 2 with the selected estimates provided by SEPUCs (first four columns), the reduced microstructure in Fig. 3(d) (the last but one column) and the original microstructure in Fig. 1(c) (last column). Although still within an acceptable range the Mori-Tanaka method slightly underestimates the macroscopic elastic response. This

difference would be even more pronounced if using mortar properties given by FFT simulations.

In most practical applications, however, the mastic asphalt is typically loaded beyond the elastic regime. The issue, whether the geometrical invariance of SEPUCs outlasts even for a non-linear response should be examined. This will be the principal objective of the next section.

3 Generalized Leonov model for Mastic Asphalt mixture from two-step homogenization

It has been experimentally observed [39] that both asphalt binders and asphalt mixtures exhibit a considerable dependence on the rate of loading and temperature. This phenomenon can be well described by the Generalized Leonov (GL) model. Although some experimental results point out a pressure dependent behavior of these systems, the present study is limited to a Mises-type material with negligible plastic volumetric deformation. The essential properties of the GL model are presented in the next section. Section 3.2 then summarizes the experimental program to calibrate the GL model on mastic scale. Upscaling towards macroscopic viscous properties of the GL model is then addressed in Sections 3.3 - 3.4.

3.1 Basic properties and implementation of GL model

Combing the Eyring flow model for the plastic component of the shear strain rate

$$\frac{de_p}{dt} = \frac{1}{2A} \sinh \frac{\tau}{\tau_0}, \quad (29)$$

with the elastic shear strain rate de_e/dt yields the one-dimensional Leonov constitutive model [40]

$$\frac{de}{dt} = \frac{de_e}{dt} + \frac{de_p}{dt} = \frac{de_e}{dt} + \frac{\tau}{\eta(de_p/dt)}, \quad (30)$$

where the shear-dependent viscosity η is provided by

$$\eta(de_p/dt) = \frac{\eta_0 \tau}{\tau_0 \sinh(\tau/\tau_0)} = \eta_0 a_\sigma(\tau). \quad (31)$$

In Eq. (29), A and τ_0 are material parameters; a_σ that appears in Eq. (31) is the stress shift function with respect to the zero shear viscosity η_0 (viscosity corresponding to a viscoelastic response). Clearly, the phenomenological representation of Eq. (30) is the Maxwell model with the variable viscosity

η . Experimental evidence proving analogy between stress and temperature allows us to extend Eq. (31) by adding a temperature (T) dependent shift factor a_T to get

$$\eta(\mathrm{d}e_p/\mathrm{d}t) = \eta_0 a_\sigma(\tau) a_T(T). \quad (32)$$

To describe multi-dimensional behavior of the material, the generalized compressible Leonov model, equivalent to the generalized Maxwell chain model, can be used [41]. The viscosity term corresponding to the μ -th unit receives the form

$$\eta_\mu = \eta_{0,\mu} a_\sigma(\tau_{\mathrm{eq}}) a_T(T), \quad (33)$$

where the equivalent shear stress τ_{eq} is provided by

$$\tau_{\mathrm{eq}} = \sqrt{\frac{1}{2} \mathbf{s} : \mathbf{s}}, \quad (34)$$

and \mathbf{s} is the deviatoric stress tensor. Admitting only small strains and isotropic material, a set of constitutive equations defining the generalized compressible Leonov model can be written as

$$\sigma_m = K \varepsilon_v, \quad (35)$$

$$\frac{\mathrm{d}\mathbf{s}}{\mathrm{d}t} = \sum_{\mu=1}^M 2G_\mu \left(\frac{\mathrm{d}\mathbf{e}}{\mathrm{d}t} - \frac{\mathrm{d}\mathbf{e}_{p,\mu}}{\mathrm{d}t} \right), \quad \mathbf{s} = \sum_{\mu=1}^M \mathbf{s}_\mu, \quad (36)$$

$$\mathbf{s}_\mu = 2\eta_\mu \frac{\mathrm{d}\mathbf{e}_{p,\mu}}{\mathrm{d}t} = 2\eta_{0,\mu} a_\sigma(\tau_{\mathrm{eq}}) a_T(T) \frac{\mathrm{d}\mathbf{e}_{p,\mu}}{\mathrm{d}t}, \quad (37)$$

where σ_m is the mean stress, ε_v is the volumetric strain, K is the bulk modulus and G_μ is the shear modulus of the μ -th unit.

While a fully implicit scheme has been implemented in [21] to integrate the system of Eqs. (35) - (37), a fully explicit Euler forward (EF) integration scheme is adopted here for simplicity. Thus to avoid numerical instabilities a relatively short time step must be prescribed. This is merely attributed to the fact that viscous parameters vary nonlinearly with stress, but in the context of EF scheme are assumed constant over the time step.

Provided that the total strain rate is constant during integration a new state of stress in the matrix phase at the end of the current time step assumes the form

$$\sigma_m(t_i) = \sigma_m(t_{i-1}) + K \Delta \varepsilon_v, \quad (38)$$

$$\{\mathbf{s}(t_i)\} = \{\mathbf{s}(t_{i-1})\} + 2\hat{G}(t_{i-1}) [\mathbf{Q}] \{\Delta \mathbf{e}\} + \{\Delta \lambda(t_{i-1})\}, \quad (39)$$

where t_i is the current time at the end of the i -th time increment; σ_m is the elastic mean stress, $\{\mathbf{s}\}$ stores the deviatoric part of the stress vector $\{\sigma\}$ and

$\{\Delta \mathbf{e}\}$ is the deviatoric part of the total strain increment. Assuming the shear relaxation modulus $\hat{G}(t)$ can be represented by a Dirichlet series expansion in the form

$$\hat{G}(t) = \sum_{\mu=1}^M G_{\mu} \exp \left(-\frac{t}{\theta_{\mu} a_{\sigma} a_T} \right), \quad (40)$$

and with reference to the EF integration scheme the time dependent variables at time instant t_{i-1} receive the form

$$\hat{G} = \sum_{\mu=1}^M G_{\mu} \frac{\theta_{\mu} a_{\sigma}(t_{i-1}) a_T(t_{i-1})}{\Delta t} \left[1 - \exp \left(-\frac{\Delta t}{\theta_{\mu} a_{\sigma}(t_{i-1}) a_T(t_{i-1})} \right) \right], \quad (41)$$

$$\{\Delta \lambda\} = - \sum_{\mu=1}^M \left[1 - \exp \left(-\frac{\Delta t}{\theta_{\mu} a_{\sigma}(t_{i-1}) a_T(t_{i-1})} \right) \right] \{\mathbf{s}_{\mu}(t_{i-1})\}, \quad (42)$$

where G_{μ} represents the elastic shear modulus in the μ -th unit of the Maxwell chain model, θ_{μ} is the associated relaxation time, $\{\mathbf{s}_{\mu}(t_{i-1})\}$, $\mu = 1, 2, \dots, M$, is the deviatoric stress vector in individual units evaluated at the beginning of the new time increment $\Delta t = t_i - t_{i-1}$, and M is the assumed number of Maxwell units in the chain model; $a_{\sigma}(t_{i-1})$ and $a_T(t_{i-1})$ are the stress and temperature shift factors, respectively. The relaxation shear moduli G_{μ} are found from a Dirichlet series expansion of creep compliance function presented, e.g. in Fig. 10(c) by invoking the correspondence principle. An example of a direct application of this principle is given in Appendix.

According to Eq. (31) the stress shift factor a_{σ} reads

$$a_{\sigma}(t_{i-1}) = \frac{\tau_{eq}(t_{i-1})}{\tau_0} / \sinh \frac{\tau_{eq}(t_{i-1})}{\tau_0}, \quad (43)$$

where the equivalent stress $\tau_{eq}(t_{i-1})$ follows from

$$\tau_{eq}(t_{i-1}) = \sqrt{\frac{1}{2} \{\mathbf{s}(t_{i-1})\}^T [\mathbf{Q}]^{-1} \{\mathbf{s}(t_{i-1})\}}, \quad (44)$$

and

$$[\mathbf{Q}] = \text{diag} \left[1, 1, 1, \frac{1}{2}, \frac{1}{2}, \frac{1}{2} \right]. \quad (45)$$

The temperature shift factor is fitted to Williams-Landel-Ferry (WLF) equation written as

$$a_T = \exp \left(\frac{-C_1(T - T_0)}{C_2 + (T - T_0)} \right), \quad (46)$$

where C_1, C_2 are model parameters, T_0 is the reference temperature and T is the actual temperature.

3.2 Rate and temperature dependent behavior of mastic from laboratory experiments

Referring to [42] we anticipated to derive the model parameter τ_0 , needed in turn for the determination of the shift factor a_σ , from a set of experiments when loading individual specimens in shear at constant strain rate. The available experimental devices, however, failed to provide the required viscous flow at zero elastic strain increment [41]. Additional difficulties in controlling the applied normal pressure when twisting the specimens immediately promoted the following alternative approach:

- Construction of the compliance master curve from the measurements of dynamic moduli at a selected range of frequencies and temperatures to first get the parameters of Eq. (46) approximating the temperature shift factor a_T .
- Determination of the model parameter τ_0 in Eq. (43) by horizontally shifting the experimentally derived compliance functions obtained from creep measurements for a given temperature at various stress levels.

The experimental program for the determination of frequency characteristics of the mastic phase was carried out jointly at the Central laboratory of Eurovia Services, Ltd. and the department of Road Structures at the Faculty of Civil Engineering, Czech Technical University in Prague. Standard dynamic shear rheometer (DSR) tests were conducted under cyclic loading undergoing a temperature and frequency sweep from 0 to 80°C and 0.1 to 100 Hz, respectively. For low temperature tests (from 0 to 20°C) a mastic film was placed between two plates (a lower fixed and an upper oscillating) of diameter $d = 8$ mm and pressed to maintain a constant height $h = 2$ mm during oscillations. For high temperatures (from 30°C to 80°C) the d/h ratio equal to 25/1 mm was used. The examined mastic consisted of 37% of limestone filler and 62,5% of polybitumen AMe 65 asphalt with bulk density $\rho_m = 1025 \text{ kgm}^{-3}$. The filler aggregates were in the following grading range: 2 mm sieve - 100%, 0.125 mm sieve - 81.1%, 0.063 mm sieve - 70.3%, with $\rho_s = 2730 \text{ kgm}^{-3}$.

The storage (G') and loss (G'') dynamic moduli were found by loading a mastic specimen in shear under strain controlled regime

$$\gamma = \bar{\gamma} \sin(t\omega), \quad \text{resulting in} \quad \tau = \bar{\tau} \sin(t\omega + \delta), \quad (47)$$

where $\bar{\gamma}$ and ω are the prescribed shear strain and angular frequency, respectively, and δ represents the phase shift between stress and strain. The

corresponding moduli then follow from

$$G' = \frac{\bar{\tau}}{\bar{\gamma}} \cos(\delta), \quad G'' = \frac{\bar{\tau}}{\bar{\gamma}} \sin(\delta). \quad (48)$$

The frequency sweep was selected such as to keep the resulting stresses within the viscoelastic limit.

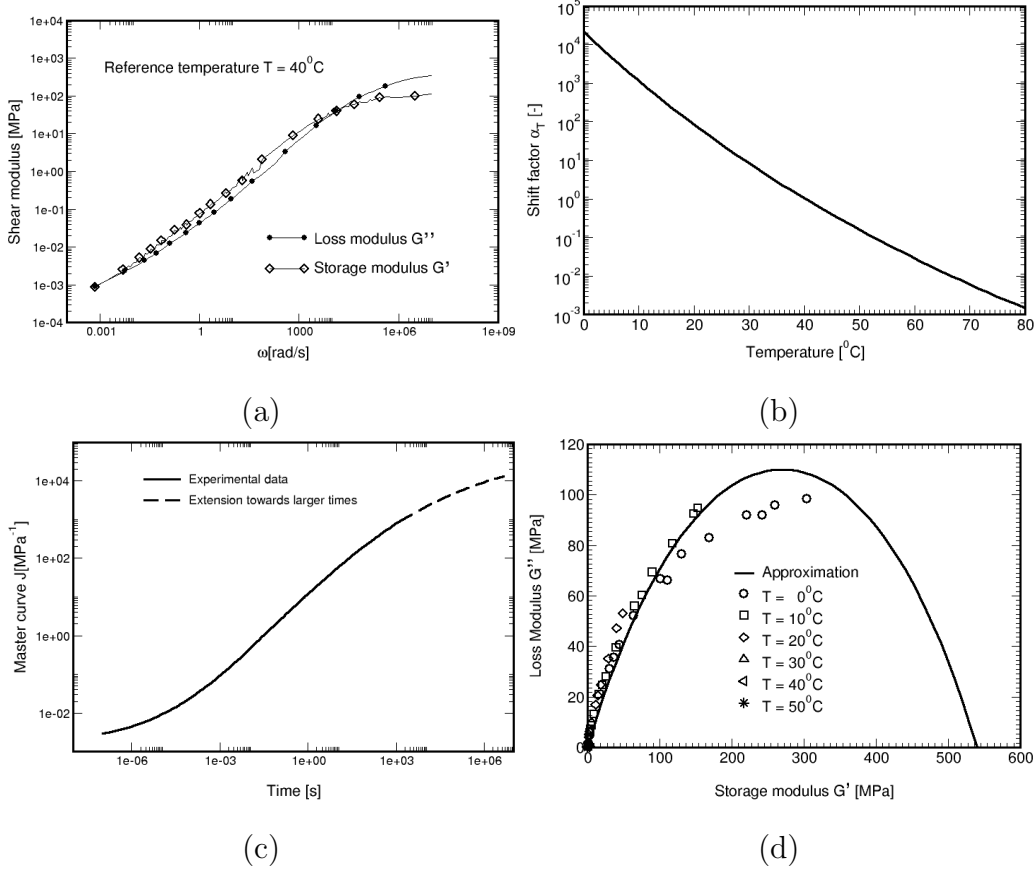


Fig. 10. (a) Dynamic moduli, (b) Shift factor, (c) Master curve, (d) Cole Cole graph

The master curves of dynamic shear moduli were constructed by superimposing the dynamic data measured at different temperatures for a given range of frequencies. Accepting the temperature superposition principle the resulting master curves seen in Fig. 10(a) were simply derived by horizontally shifting individual curves to comply with the data one would obtain for the 40°C reference temperature at much longer (data for temperatures above 40°C) or shorter (data for temperatures below 40°C) times if performing standard creep measurements. The dynamic moduli master curves were subsequently converted into a time-dependent compliance function at 40°C employing the Fourier transform. The result appears in Fig. 10(c). For the available temperature range the resulting master curve can reliably cover the viscoelastic creep response over the time span up to 1000 s. To enhance numerical stability this curve was artificially prolonged by two additional decades, see the

dashed line in Fig. 10(c). The associated temperature dependent variation of shift factor a_T fitted to Eq. (46) is plotted in Fig. 10(b). The corresponding parameters are stored in Table 3. Finally, The experimentally-obtained values of G' and G'' are plotted in the so-called Cole-Cole diagram in Fig. 10(d) used in the present study to estimate the elastic modulus of mastic phase, recall Section 2.2.4. Note that the master curves in Figs. 10(a),(c) were provided directly by a built in software of DSR devices.

The second class of experiments delivered the creep data at constant temperature $T = 30^{\circ}\text{C}$ but at different magnitudes of the applied load. These data together with the previous results enabled us to obtain the necessary parameter τ_0 . To that end, the original master curve in Fig. 10(c) was first converted to comply with the one for 30°C . A horizontal shift of four available creep compliance functions finally served to estimate the parameter τ_0 , see Table 3. Additional creep experiments performed at temperature 50°C were used to validate not only the estimated value of τ_0 but also the temperature-stress superposition principle expressed, with reference to so called reduced time, as

$$\varphi_t = \int_0^t \frac{dt}{a_T[T(t)] \times a_\sigma[\tau_{eq}(t)]}. \quad (49)$$

The results shown in Fig. 11 confirm applicability of the GL model to well represent the temperature and rate dependent behavior of mastic material.

Table 3

Model parameters of Eqs. (31) and (46)

Scale	T_0	C_1	C_2	τ_0 [Pa]
Mastic	40°C	38.56	195.42	1150
Mortar	40°C	38.56	195.42	2600
MAm	40°C	38.56	195.42	2951

Further support for the use of GL model can be gained from the results presented in Fig. 12. Therein, the numerical predictions of static behavior at different strain rates and temperatures are compared with experimentally obtained data. Note that this set of experiments was not considered to calibrate the material model. Realizing a difficulty of performing reproducible tests with such a material suggests almost a “remarkable” match.

3.3 Response of mortar from virtual experiments

Following on the heels of experimental work discussed in the previous section, a virtual set of experiments is proposed to arrive at a homogenized master curve and associated temperature and stress dependent shift factors on the

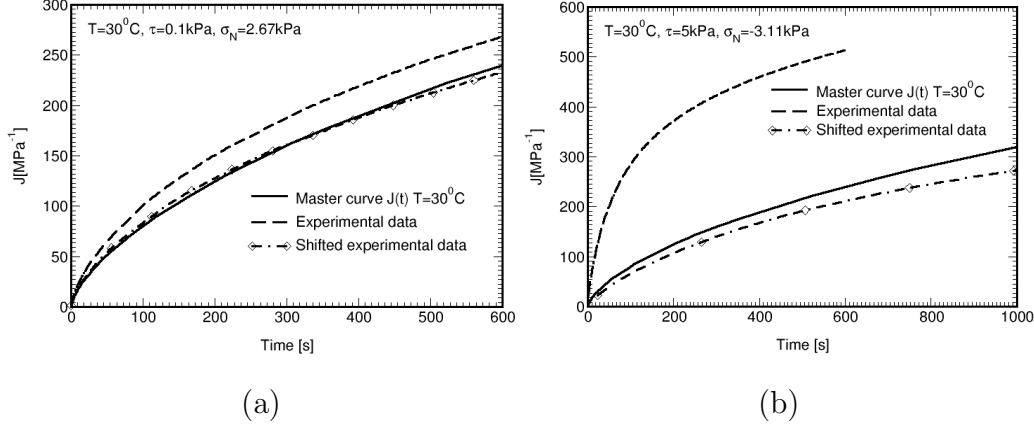


Fig. 11. Model performance - effect of the applied stress level : (a) $\tau = 100\text{Pa}$, (b) $\tau = 5000\text{Pa}$

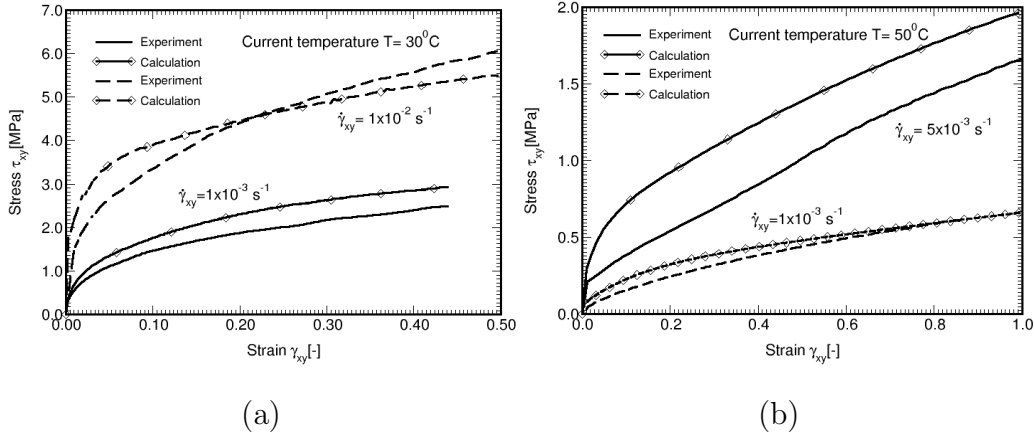


Fig. 12. Tensile loading at constant strain rate - experimental measurements vs. numerical predictions: (a) $T = 30^\circ\text{C}$, (b) $T = 50^\circ\text{C}$

scale of mortar. To be consistent with Section 2.3 the PUC in Fig. 5(d) is chosen to represent an RVE for numerical analysis. The concept of first order homogenization of periodic fields outlined in Section 2.2.3 is given the preference to deliver the homogenized creep response of the mortar phase at different temperature and stress levels.

First, a uniformly distributed range of temperatures from 0°C to 100°C was considered to provide for a temperature dependent viscoelastic behavior of mortar loaded in shear by the remote stress $\Sigma_{yx} = 1\text{kPa}$. Individual curves plotted in Fig. 13(a) were then horizontally shifted to give the homogenized creep compliance master curve seen in Fig. 13(b) and consequently estimates of the parameters of WLF equation (46). The parameters C_1, C_2 for the reference temperature $T = 40^\circ\text{C}$ are stored in Table. 3 surprisingly suggesting no differences between individual scales. The stiffening, observed for high temperatures, is attributed to a volumetric locking owing to a very low shear modulus approaching to zero. This in turn yields the Poisson ratio close to 0.5

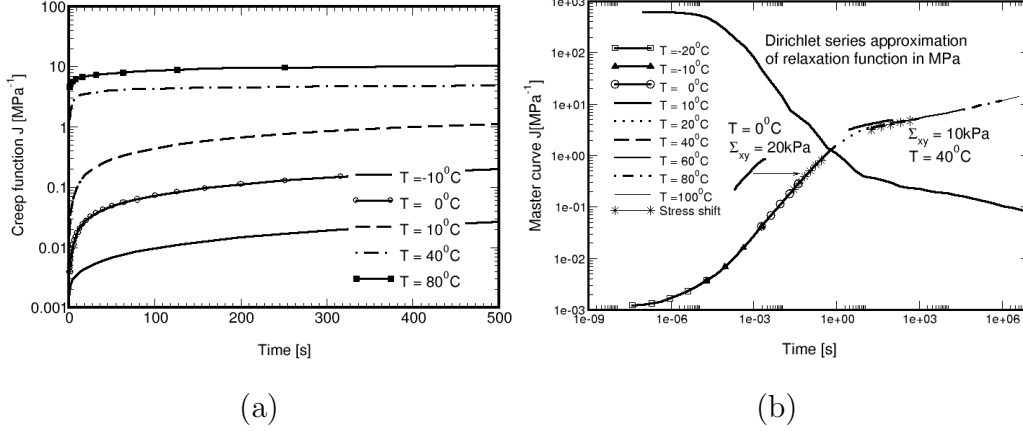


Fig. 13. (a) Creep data at different temperatures for reference stress $\Sigma_{xy} = 1\text{kPa}$, (b) Master curve for reference temperature $T = 40^\circ\text{C}$

in a finite zone of the binder phase that is progressed over the entire unit cell as seen in Fig. 13(b). Note that such a microstructure dependent response can hardly be represented by the Mori-Tanaka method, see appendix for further illustration.

The second set of creep experiments was conducted at two different temperatures and two different levels of the remote stress Σ_{xy} . The two representative results, $[40^\circ\text{C}, 10\text{kPa}]$ and $[0^\circ\text{C}, 20\text{kPa}]$, are plotted as solid lines in Fig. 13(b). The indicated horizontal shifts identified with the corresponding star-lines then supplement the necessary data for the derivation of stress dependent shift factor a_σ fitted to Eq. (43). The searched parameter τ_0 is available in Table. 3. Note that prior to shifting the curves the result derived for 0°C was thermally adjusted to be consistent with the 40°C master curve.

3.4 Response of MAm from virtual experiments

Derivation of the macroscopic creep compliance master curve for a Mastic Asphalt mixture follows the general scheme sketched in the previous section. A statistically equivalent periodic unit cell introduced in Section 2.3 is considered for numerical simulations. The principal assumption of restricting the material model on every scale to one particular format is brought to light here by suggesting the binder be well represented by the homogenized GL model predicted on the mortar scale.

However, for problems involving significant nonlinearities, the fundamental statement borrowed from elasticity solutions that any statistically equivalent periodic unit cell is equally suitable should be scrutinized first.

To address this issue the statistically equivalent unit cells in Fig. 8 were sub-

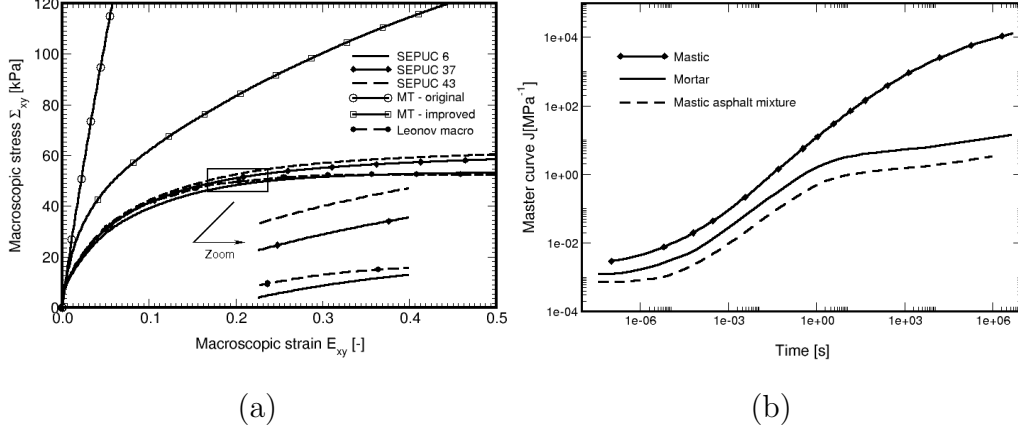


Fig. 14. (a) Macroscopic response for various SEPUCs $T = 20^\circ\text{C}$, $\dot{E}_{xy} = 10^{-4}$, (b) Master curves on individual scales for reference temperature $T = 40^\circ\text{C}$

jected to a remote shear strain rate $\dot{E}_{xy} = 10^{-4}$. The resulting homogenized stress-strain curves for temperature $T = 20^\circ\text{C}$ are shown in Fig. 14(a). Although no “perfect match” is observed, the difference in estimated load bearing capacities is in the same range as the predicted elastic constants, see e.g. Table 2, not exceeding 10%. On the contrary, the distribution of local fields varies considerably as seen in Fig. 15. While a highly localized distribution of shear strain γ_{xy}^m in the mortar phase, identified with the lowest bearing capacity in Fig. 14(a), is evident in Fig. 15(a), the variation of this quantity in Fig. 15(c) shows a rather distributed character consequently resulting in a slightly stiffer response on the macroscale.

Although certainly more accurate, the detailed finite element simulations are in general computationally very expensive and often call for less demanding alternatives such as the Mori-Tanaka method. Unfortunately, the corresponding results also plotted in Fig. 14(a) clearly expose essential limitations of two-point averaging schemes, unable to capture localization phenomena observed in composites with a highly nonlinear response of the binder phase [21]. On that ground, a considerably more refined variant of the TFA method would be necessary [43,44]. In this paper, however, the attention is limited to a two-phase composite only as discussed in Section 2.2.1. The presented results in Fig. 14(a) correspond to a classical formulation with the localization and transformation tensors calculated only once being functions of elastic properties of individual constituents (MT-original), and to the formulation where these tensors are updated after each time step taking into account increasing compliance of the mortar phase with time (MT-improved). Note that even the latter case produces much stiffer response, although at a fraction of time, when compared to the FE results.

Regarding the “similarity” of macroscopic response from various SEPUCs, the SEPUC No. 37 was selected to provide data needed in the calibration of the

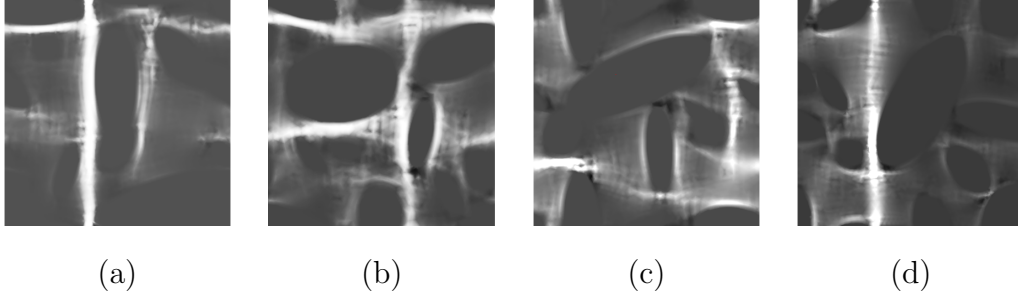


Fig. 15. Distribution of local shear strain: (a) SEPUC 6, (b) SEPUC 37, (c) SEPUC 43, (d) SEPUC 48

macroscopic GL model. Virtual numerical tests identical to those in Section 3.3 were again performed to give first the homogenized master curve displayed in Fig. 14(b) and consequently the model parameters of Eqs. (43) and (46) available in Table 3. Note again the same temperature shift as obtained already for lower scales. This is evident in Fig. 14(b) showing only vertical shift of individual master curves attributed to an increasing stiffness when moving up individual scales.

Finally, fitting the inverse of the homogenized master curve to a particular chain of Maxwell units then allows for estimating the macroscopic response of MAm to a given load limiting the material symmetry to a macroscopic isotropy. The response of the homogenized asphalt mixture to the applied remote shear strain labeled as “Leonov macro” appears in Fig. 14(a). Since derived from the solution of a unit cell problem, a relatively good agreement with these solutions has been expected. The difference is merely attributed to the specific approximation of the homogenized master curve via Dirichlet series. It is fair to mention a considerable sensitivity of the predictions to a particular choice of pairs of parameters (shear modulus and retardation time) of the Maxwell units. Although promising, to fully accept the proposed uncoupled multiscale computational strategy will require further testing, both numerical and laboratory. This topic is still widely opened.

4 Conclusions

Although research interests on flexible pavements have been quite intense in the past two decades, the field is still very much in development and will certainly witness considerable activity in the coming decade particular in connection to hierarchical modeling and micromechanics. Within this framework, the present contribution provides theoretical tools for the formulation of macroscopic constitutive law reflecting the confluence of threads coming from experimental work, image analysis, statistical mechanics and traditional disciplines of micromechanics and the first order computational homogenization. Here,

the totally uncoupled multiscale modeling approach is favored to enable an inexpensive analysis of real world large scale structures. Since much of the considered is primarily computational it would be audacious to brought this approach directly to points of application without additional experimental validation. Large scale experiments of rut depth measurements due to moving wheel load are currently under way. The effect of microstructure anisotropy, influence of the first stress invariant or three-dimensional character of asphalt mixtures are just a few issues which need to be addressed, yielding flexible pavements a fertile field of future research.

Acknowledgements

This outcome has been achieved with the financial support of the Ministry of Education, Youth and Sports, project No. 1M0579, within activities of the CIDEAS research centre.

A The Mori-Tanaka predictions based on correspondence principle

The correspondence principle as a tool allowing for interconversion of linear viscoelastic response functions has already been mention in Section 3.1. Although not used in the present contribution, this principle is reviewed here to fill in the list of possible routes for deriving the homogenized viscoelastic response of composites using simple averaging schemes. As an example, the Mori-Tanaka method is adopted again to construct the homogenized master curve of a two-phase composite medium composed of aligned elastic circular fibers bonded to a viscoelastic mastic phase. This approach thus allows direct comparison with the finite element predictions obtained on the mortar scale.

Consider a homogenized relaxation loading path written as

$$\Sigma_{xy}(t) = G_{\text{hom}}(t) E_{xy}, \quad (\text{A.1})$$

$$G_{\text{hom}}(t) = \sum_{\mu=1}^M G_{\mu}^{\text{hom}} \exp \left(-\frac{t}{\theta_{\mu}^{\text{hom}} a_{\sigma}^{\text{hom}} a_T^{\text{hom}}} \right), \quad (\text{A.2})$$

where M is the number of Maxwell units representing the homogenized response, $a_{\sigma}^{\text{hom}} = 1$ in the viscoelastic regime, $a_T^{\text{hom}} = 1$ for the reference temperature $T = 40^{\circ}\text{C}$ (assumptions complying with the corresponding master curve shown in Fig. 13(b)) and $\theta_{\mu}^{\text{hom}}$ are appropriate relaxation times. Then, according to the correspondence principle the Laplace-Carson transform of Eq. (A.1) gives

$$\Sigma_{xy}^*(p) = G_{\text{hom}}^*(p) E_{xy}^*(p), \quad (\text{A.3})$$

$$G_{\text{hom}}^*(p) = \sum_{\mu=1}^M \frac{G_{\mu}^{\text{hom}}}{\left(\frac{1}{\theta_{\mu}^{\text{hom}}} + p\right)}. \quad (\text{A.4})$$

Following [15] provides Eq. (12) in the Laplace space in the form

$$m_{\text{MT}}^* = \frac{m_s^* m_m^* (k_m^* + 2m_m^*) + k_m^* m_m^* (c_s m_s^* + c_m m_m^*)}{k_m^* m_m^* + (k_m^* + 2m_m^*) (c_s m_s^* + c_m m_m^*)}, \quad (\text{A.5})$$

Since the volumetric response is assumed to remain elastic, recall Eq. (35), we get

$$k_s^*(p) = \frac{m_s^*}{(1 - 2\nu_s)}, \quad m_s^* = \frac{m_s}{p}, \quad (\text{A.6})$$

$$k_m^*(p) = \frac{m_m^{el}}{p(1 - 2\nu_m)}, \quad m_m^{el} = \sum_{\mu=1}^N G_{\mu}^m, \quad (\text{A.7})$$

$$m_m^*(p) = \sum_{\mu=1}^N \frac{G_{\mu}^m}{\left(\frac{1}{\theta_{\mu}^m} + p\right)}. \quad (\text{A.8})$$

where N is the number of Maxwell units approximating the behavior of the mastic phase and $a_{\sigma}^m = a_T^m = 1$ is again adopted to guarantee compatibility with the results presented in Section 3.2. Once the Mori-Tanaka estimate G_{MT} of the homogenized relaxation function G_{hom} in the Laplace space are known, the desired coefficients G_{μ}^{hom} , which enter Eq. (A.2), are found by solving the following minimization problem

$$E_G = \sum_{p_k}^K [G_{\text{MT}}^*(p_k) - G_{\text{hom}}^*(p_k)]^2 = \min, \quad (\text{A.9})$$

thereby avoiding a cumbersome and rather unstable numerical transformation of Eq. (A.5) back to time dependent solution (A.2). Solution strategies based on soft computing [37,45,38] are typically employed to solve Eq. (A.9).

Given the relationship between relaxation and compliance functions

$$pJ^*(p) = \frac{1}{pG^*(p)}, \quad (\text{A.10})$$

allows us to write a dual representation of Eq. (A.5) in the form

$$p^2 J_{\text{MT}}^*(p) = \frac{1}{m_{\text{MT}}^*} = \frac{\frac{k_m^*}{p^2 J_m^*} + \left(k_m^* + \frac{2}{p^2 J_m^*}\right) \left(\frac{c_s}{p^2 J_m^*} + c_m m_s^*\right)}{\frac{m_s^*}{p^2 J_m^*} \left(k_m^* + \frac{2}{p^2 J_m^*}\right) + \frac{k_m^*}{p^2 J_m^*} \left(c_s m_s^* + \frac{c_m}{p^2 J_m^*}\right)}, \quad (\text{A.11})$$

where

$$J_m^*(p) = \sum_{\mu=1}^N \frac{J_\mu^m}{p(p\tau_\mu^m + 1)}. \quad (\text{A.12})$$

The homogenized coefficients $J\mu^{\text{hom}}$ then follow from the minimization of a dual error function

$$E_J = \sum_{p_k}^K [J_{\text{MT}}^*(p_k) - J_{\text{hom}}^*(p_k)]^2 = \min. \quad (\text{A.13})$$

or directly from Eq. (A.10) providing the set of coefficients $G\mu^{\text{hom}}$ has been already found from the primary formulation.

The resulting MT prediction of J_{MT} for the reference temperature $T = 40^\circ\text{C}$ is compared in Fig. A.1(b) with the PUC solution on the mortar scale, recall Fig. 13(b). Inability of the MT method to capture the stiffening effect already mentioned in Section 3.3 is evident in both the Laplace and time space. It is interesting to point out that such a discrepancy appears already for the elastic predictions if setting $m_m \rightarrow 0$ and $\nu_m \rightarrow 0.5$, in which case the binder behaves as an incompressible fluid.

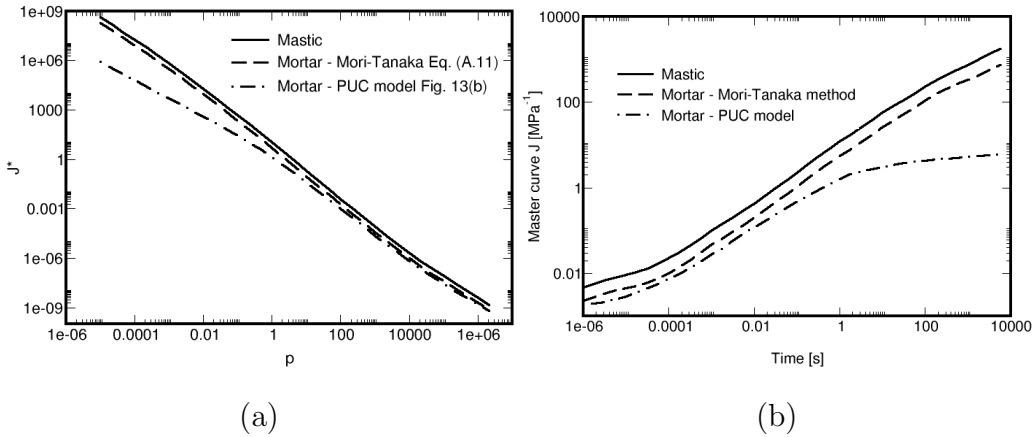


Fig. A.1. (a) Laplace transform of the compliance function, (b) Master curve for reference temperature $T = 40^\circ\text{C}$

References

- [1] E. Masad, L. Tashman, D. Little, H. Zbib, Viscoplastic modelling of asphalt mixes with effects of anisotropy, damage and aggregate characteristics, *Mechanics of Materials* 37 (2005) 1242–1256. doi:10.1016/j.mechmat.2005.06.003.
- [2] V. Panoskaltsis, D. Panneerselvam, An anisotropic hyperelastic-viscoplastic damage model for asphalt concrete materials and its numerical implementation, in: 5th GRAM International Congress on Computational Mechanics, Limassol, 2005.
- [3] J. Sousa, S. Weissman, J. Sackman, C. Monismith, Nonlinear elastic viscous with damage model to predict permanent deformation of asphalt concrete mixes, *Transportation Research Record No. 1384: Journal of the Transportation Research Board*, Washington, D.C. (1993) 80–93 Available from: <http://pubsindex.trb.org/document/view/default.asp?lbid=378429>.
- [4] J. Sousa, S. Weissman, Modeling permanent deformation of asphalt concrete mixtures, *Journal Association of of Asphalt Paving Technologists* 63 (1994) 225–257.
- [5] S. Weissman, J. Sackman, J. Harvey, I. Guada, A constitutive law for asphalt concrete mixes formulated within the realm of large strains, in: 16th Engineering Mechanics Conference, University of Washington, Seattle, 2003. Available from: <http://www.ce.washington.edu/em03/proceedings/papers/166.pdf>.
- [6] B. Huang, L. Mohammad, W. Wathugala, Application of temperature dependent viscoplastic hierarchical single surface model for asphalt mixtures, *Journal of Materials in Civil Engineering* 16 (2) (2004) 147–154. doi:10.1061/(ASCE)0899-1561(2004)16:2(147).
- [7] H. Fang, J. Haddock, T. White, A. Hand, On the characterization of flexible pavement rutting using creep model-based finite element analysis, *Finite Element in Analysis and Design* 41 (2004) 49–73. doi:10.1016/j.finel.2004.03.002.
- [8] A. Papagiannakis, A. Abbas, E. Masad, Microemchanical analysis of viscoelastic properties using image analysis, *Transportation Research Record No. 1789: Journal of the Transportation Research Board*, Washington, D.C. (2002) 113–120.
- [9] A. Abbas, A. Papagiannakis, E. Masad, Linear and nonlinear viscoelastic analysis of the microstructure of asphalt concretes, *Journal of Materials in Civil Engineering* 16 (2) (2004) 147–154. doi:10.1061/(ASCE)0899-1561(2004)16:2(133).
- [10] Z. You, S. Adhikari, M. Kutay, Dynamic modulus simulation of the asphalt concrete using the X-ray computed tomography images, *Materials and Structures* 42 (2006) 617–630. doi:10.1617/s11527-008-9408-4.

- [11] Q. Dai, M. Saad, Z. You, A micromechanical finite element model for linear and damage-coupled viscoelastic behaviour of asphalt mixture, *International Journal for Numerical and Analytical Methods in Geomechanics* 30 (2006) 1135–1158. doi:10.1002/nag.520.
- [12] R. Lackner, R. Blab, A. Jager, M. Spiegl, K. Kappl, M. Wistuba, B. Gagliano, J. Eberhardsteiner, Multiscale modeling as the basis for reliable predictions of the behaviour of multi-composed materials, in: B. Topping, C. M. Soares (Eds.), *Progress in Engineering Computational Technology*, Saxe-Coburg Publications, Stirling, Scotland, 2004, pp. 153–187.
- [13] R. Lackner, M. Spiegl, R. Blab, J. Eberhardsteiner, Is low-temperature creep of asphalt mastic independent of filler shape and mineralogy? - arguments from multiscale analysis, *Journal of Materials in Civil Engineering*, ASCE 15 (2005) 485–491. doi:10.1061/(ASCE)0899-1561(2005)17:5(485).
- [14] R. Lackner, R. Blab, J. Eberhardsteiner, H. Mang, Characterization and multiscale modeling of asphalt - Recent developments in upscaling of viscous and strength properties, in: *III European Conference on Computational Mechanics*, 2006, p. 26. doi:10.1007/1-4020-5370-3_26.
- [15] E. Aiger, C. Pichler, R. Lackner, Bottom-up multiscale modeling of viscoelastic properties of asphalt, in: S. . A.-Q. Loizos (Ed.), *Advanced Characterisation of Pavement and Soil Engineering Materials*, 2007 Taylor & Francis Group, London, ISBN 978-90-1234-1234, 2004.
- [16] K. Matouš, M. Lepš, J. Zeman, M. Šejnoha, Applying genetic algorithms to selected topics commonly encountered in engineering practice, *Computer Methods in Applied Mechanics and Engineering* 190 (13–14) (2000) 1629–1650. doi:10.1016/S0045-7825(00)00192-4.
- [17] J. Zeman, M. Šejnoha, Numerical evaluation of effective properties of graphite fiber tow impregnated by polymer matrix, *Journal of the Mechanics and Physics of Solids* 49 (1) (2001) 69–90. doi:10.1016/S0022-5096(00)00027-2.
- [18] M. Šejnoha, J. Zeman, Overall viscoelastic response of random fibrous composites with statistically quasi uniform distribution of reinforcements, *Computer Methods in Applied Mechanics and Engineering* 191 (44) (2002) 5027–5044. doi:10.1016/S0045-7825(02)00433-4.
- [19] J. Zeman, M. Šejnoha, From random microstructures to representative volume elements, *Modelling and Simulation in Materials Science and Engineering* 15 (4) (2007) S325–S335. doi:10.1088/0965-0393/15/4/S01.
- [20] Z. Bittnar, Šejnoha J., *Numerical methods in structural engineering*, ASCE Press, 1996.
- [21] M. Šejnoha, R. Valenta, J. Zeman, Nonlinear viscoelastic analysis of statistically homogeneous random composites, *International Journal for Multiscale Computational Engineering* 2 (4) (2004) 645–673. doi:10.1615/IntJMultCompEng.v2.i4.

- [22] J. Šejnoha, M. Šejnoha, J. Zeman, J. Sýkora, J. Vorel, Mesoscopic study on historic masonry, *Structural Engineering and Mechanics* 30 (1) (2008) 99–117. [arXiv:0803.3262](#).
- [23] G. J. Dvorak, Y. Benveniste, On transformation strains and uniform fields in multiphase elastic media, *Proceedings of the Royal Society of London Series A - Mathematical, Physical and Engineering Sciences* 437 (1900) (1992) 291–310.
- [24] G. J. Dvorak, Transformation field analysis of inelastic composite materials, *Proceedings of the Royal Society of London Series A - Mathematical, Physical and Engineering Sciences* 437 (1900) (1992) 311–327. [doi:10.1098/rspa.1992.0062](#).
- [25] T. Mori, K. Tanaka, Average stress in matrix and average elastic energy of elastic materials with misfitting inclusions, *Acta Metallurgica* 21 (1973) 571. [doi:10.1016/0001-6160\(73\)90064-3](#).
- [26] Y. Benveniste, A new approach to the application of Mori-Tanaka theory in composite materials, *Mechanics of Materials* 6 (1987) 147–157. [doi:10.1016/0167-6636\(87\)90005-6](#).
- [27] T. Mura, *Micromechanics of Defects in Solids*, second revised Edition, no. 3 in *Mechanics of elastic and inelastic solids*, Kluwer Academic Publishers, 1987.
- [28] H. Moulinec, P. Suquet, Micromechanics of materials: From numerical simulations to predictive models, in: J. K. N. Avaras (Ed.), *3rd National Congress on Computational Mechanics*, 1999, pp. 93–100.
- [29] Z. Hashin, S. Shtrikman, On some variational principles in anisotropic and nonhomogeneous elasticity, *Journal of the Mechanics and Physics of Solids* 10 (1962) 335–342. [doi:10.1016/0022-5096\(62\)90004-2](#).
- [30] J. R. Willis, Bounds and self-consistent estimates for the overall properties of anisotropic composites, *Journal of the Mechanics and Physics of Solids* 25 (1977) 185–202.
- [31] M. J. Beran, *Statistical Continuum Theories*, *Monographs in Statistical Physics*, Interscience Publishers, 1968.
- [32] J. C. Michel, H. Moulinec, P. Suquet, Effective properties of composite materials with periodic microstructure: A computational approach, *Computer Methods in Applied Mechanics and Engineering* 172 (1999) 109–143. [doi:10.1016/S0045-7825\(98\)00227-8](#).
- [33] R. Hill, Elastic properties of reinforced solids - Some theoretical principles, *Journal of the Mechanics and Physics of Solids* 11 (1963) 357–372. [doi:10.1016/0022-5096\(63\)90036-X](#).
- [34] J. Fish, K. Shek, Multiscale analysis of large-scale nonlinear structures and materials, *International Journal for Computational Civil and Structural Engineering* 1 (1) (2000) 79–90.

- [35] V. Kouznetsova, M. G. D. Geers, W. A. M. Brekelmans, Multi-scale constitutive modelling of heterogeneous materials with a gradient-enhanced computational homogenization scheme, *International Journal for Numerical Methods in Engineering* 54 (8) (2002) 1235–1260. doi:10.1002/nme.541.
- [36] S. Torquato, *Random heterogeneous materials: Microstructure and macroscopic properties*, Springer-Verlag, 2002.
- [37] A. Ibrahimbegović, C. Knopf-Lenoir, A. Kučerová, P. Villon, Optimal design and optimal control of structures undergoing finite rotations and elastic deformations, *International Journal for Numerical Methods in Engineering* 61 (14) (2004) 2428–2460. arXiv:0902.1037, doi:10.1002/nme.1150.
- [38] A. Kučerová, Identification of nonlinear mechanical model parameters based on softcomputing methods, Ph.D. thesis, Ecole Normale Supérieure de Cachan, Laboratoire de Mécanique et Technologie (2007). Available from: <http://tel.archives-ouvertes.fr/tel-00256025/en>.
- [39] J. Read, D. Whiteoak, *The Shell Bitumen Handbook*, 5th Edition, Thomas Telford Publishing, London, 2003.
- [40] A. I. Leonov, Non-equilibrium thermodynamics and rheology of viscoelastic polymer media, *Rheologica Acta* 15 (1976) 85–98.
- [41] T. A. Tervoort, Constitutive modeling of polymer glasses: Finite, nonlinear viscoelastic behaviour of polycarbonate, Ph.D. thesis, Eindhoven University of Technology, Eindhoven (1996).
- [42] M. Šejnoha, R. Valenta, Epoxy resin as a bonding agent in polymer matrix composites: material properties and numerical implementation, in: *Advances in Computational & Experimental Engineering & Sciences*, Forsyth: Tech Science Press, 2004.
- [43] G. J. Dvorak, Y. A. Bahei-El-Din, A. M. Wafa, Implementation of the transformation field analysis for inelastic composite-materials, *Computational Mechanics* 14 (3) (1994) 201–228. doi:10.1007/BF00370073.
- [44] J. Chaboche, S. Kruch, J. Maire, T. Pottier, Towards a micromechanics based inelastic and damage modeling of composites, *International Journal of Plasticity* 17 (4) (2001) 411–439. doi:10.1016/S0749-6419(00)00056-5.
- [45] A. Kučerová, M. Lepš, J. Zeman, Back analysis of microplane model parameters using soft computing methods, *Computer Assisted Mechanics and Engineering Science* 14 (2007) 219–242. arXiv:0902.1690.